Journal of Sol-Gel Science and Technology
https://doi.org/10.1007/s10971-024-06396-8

ORIGINAL PAPER

Dielectric and structural properties of $Co_{0.6}Zn_{0.4}Fe_2O_4$ nanoferrites: sol–gel synthesis

A. Messaoudi[1,2] · Aref Omri[2] · A. Benali[3,4] · M. A. Ghebouli[5,6] · A. Djemli[7,8] · M. Fatmi[5] · N. Hamdaoui[1] · R. Ajjel[9] · M. Habila[10] · Asma A. Alothman[10] · Saikh Mohammad[10] · B. F. O. Costa[11] · M. F. P. Graca[4] · K. Khirouni[12]

Received: 5 December 2023 / Accepted: 18 April 2024

Abstract

This study investigated the synthesis and analysis of Co–Zn nanoferrites, specifically $Co_{0.6}Zn_{0.4}Fe_2O_4$, using the sol–gel method. The morphological, structural, and electrical properties of these ferrites were explored. The $Co_{0.6}Zn_{0.4}Fe_2O_4$ spinel ferrite was synthesized using metal nitrate reagents and ethylene glycol, followed by a series of heating and sintering processes. Rietveld-refined X-ray diffraction (XRD) confirmed the crystalline structure and phase purity, revealing a monophasic spinel structure. Scanning electron microscopy (SEM) analysis showed distinct grain agglomeration and porosity, indicating the material's unique microstructure. Impedance measurements further characterized the optical and electrical properties. The electrical conductivity of $Co_{0.6}Zn_{0.4}Fe_2O_4$ demonstrated a thermally activated conduction process, adhering to Jonscher's universal power law. The complex impedance analysis revealed thermally activated behavior, confirming the presence of relaxation processes influenced by temperature. Nyquist plots indicated the contributions of grains, grain boundaries, and electrodes to the electrical behavior. The complex electrical modulus and dielectric studies provided insights into the dielectric characteristics, confirming high space charge polarization at grain boundaries and low dielectric loss. These findings suggested that $Co_{0.6}Zn_{0.4}Fe_2O_4$ nanoferrites synthesized via the sol–gel method exhibited desirable electrical and structural properties, making them promising for various technological applications.

✉ Aref Omri
omriaref@yahoo.fr

✉ M. Fatmi
fatmimessaoud@yahoo.fr

[1] Laboratory of Energy and Materials (LabEM-LR11ES34), Higher School of Science and Technology of Hammam Sousse (ESSTHS), University of Sousse, Hammam Sousse, Tunisia

[2] Laboratory of Advanced Multifunctional Materials and Technological Applications, Faculty of Science and Technology of Sidi Bouzid, University Campus Agricultural City, University of Kairouan, Sidi Bouzid 9100, Tunisia

[3] Applied Physics Laboratory, Faculty of Sciences, University of Sfax, P.O. Box 1171, Sfax 3000, Tunisia

[4] I3N and Physics Department, University of Aveiro, 3810-193 Aveiro, Portugal

[5] Research Unit on Emerging Materials (RUEM), University Ferhat Abbas of Setif 1, Setif 19000, Algeria

[6] Department of Chemistry, Faculty of Sciences, University of Mohamed Boudiaf, M'sila 28000, Algeria

[7] Faculty of Physics, University of Sciences & Technology Houari Boumediene (U.S.T.H.B), El Alia, BP 32, Bab Ezzouar, 16111 Algiers, Algeria

[8] Department of Physics, Faculty of Sciences, University of Mohamed Boudiaf, M'sila 28000, Algeria

[9] Laboratory of Metabolic Biophysics and Applied Professional and Environmental Toxicology (LR12ES02), Faculty of Medicine Ibn El Jazzar, University of Sousse, Sousse 4002, Tunisia

[10] Department of Chemistry, College of Science, King Saud University, P.O. Box 2455, Riyadh 11451, Saudi Arabia

[11] CFisUC, Physics Department, University of Coimbra, Rua Larga, 3004-516 Coimbra, Portugal

[12] Laboratory of Materials Physics and Nanomaterials Applied to the Environment, Faculty of Sciences of Gabes, Erriadh Campus, University of Gabes, 6079 Gabes, Tunisia

Published online: 20 May 2024

Graphical Abstract

Sol–gel synthesis steps for $Co_{0.6}Zn_{0.4}Fe_2O_4$ ferrite.

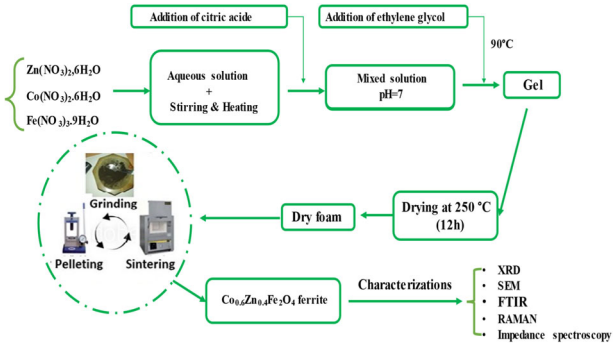

Keywords Spinel ferrites · Sol–gel synthesis · Dielectric properties · Nanomaterials

Highlights

- The sol–gel process is used to produce the nanomagnetic system $Co_{0.6}Zn_{0.4}Fe_2O_4$.
- The activation energy was evaluated using conductivity, complex impedance (Z''), and complex modulus (M''), and the obtained values are near signifying that charge carriers must overcome equivalent energy barriers while conducting and relaxing.
- The electrical conductivity of $Co_{0.6}Zn_{0.4}Fe_2O_4$ demonstrated a thermally activated conduction process, adhering to Jonscher's universal power law.

1 Introduction

Magnetic nanoparticles have been the subject of extensive research in recent years, with a particular focus on nanoferrites due to their potential applications in various technical fields [1–4]. The remarkable structural, morphological, magnetic, electrical, optical, and thermal properties of nanoferrites are driving their large-scale synthesis. These properties make them attractive for a variety of applications, such as magnetron drug delivery, medical resonance imaging, optoelectronics, magnetic sensors, and energy storage devices [5–10]. Spinel ferrite magnetic nanoparticles are of particular interest. They are composed of cubic symmetry crystals of the $MgAl_2O_4$ type, whose basic formula is AB_2O_4, where A is a divalent cation such as Sn, Mn, Fe, Co, and so on, and B is a trivalent cation such as Fe. These materials have received significant investigation due to their exceptional properties and are part of the space group Fd-3m (N° 227 in International Tables) [11]. The ferrites are an important class of ceramic materials that exhibit unique magnetic, electrical, and optical properties. Among the most commonly used ferrites are cobalt ferrite ($CoFe_2O_4$), nickel ferrite ($NiFe_2O_4$), manganese ferrite ($MnFe_2O_4$), and zinc ferrite ($ZnFe_2O_4$) [12, 13]. These ferrites are used in a wide range of applications, including permanent magnets, transformer cores, inductors, magnetic sensors, and magnetic memory devices. Mixed ferrites, which are formed by combining two or more different metals, offer a wider variety of properties and are used in specific applications. For example, cobalt–zinc ferrite ($CoZnFe_2O_4$) is used in high-frequency applications due to its low dielectric loss, while manganese–zinc ferrite ($MnZnFe_2O_4$) is used in power applications due to its high magnetic permeability [14]. Among spinel ferrites, Co–$ZnFe_2O_4$ nanoferrites are highly versatile and attractive magnetic materials. Cobalt ferrite ($CoFe_2O_4$) is especially promising for various applications, including magnetic drug delivery, high-density audio and video tapes, optical discs, and digital records, due to its strong magnetocrystalline anisotropy and excellent chemical stability [15]. The magnetic properties of $CoFe_2O_4$ are greatly influenced by appropriate diamagnetic impurity substitution [16]. Several methods have been developed for the synthesis of Co–$ZnFe_2O_4$ nanoferrites, including the ceramic technique, microwave combustion method, forced hydrolysis, coprecipitation, and sol–gel method [17–21]. Of these methods, the sol–gel method has shown remarkable potential for synthesizing spinel ferrite nanoparticles over the last 2 decades. Numerous spinel ferrite materials have been synthesized using this process, also referred to as a solution-burning methodology [22–24]. Bas du formulaire $Co_xZn_{1-x}Fe_2O_4$ nanoferrites, particularly those with Zn substitution, have garnered significant attention for their enhanced magnetic and electrical properties [25, 26]. These ferrites offer several advantages over lead-based ceramics,

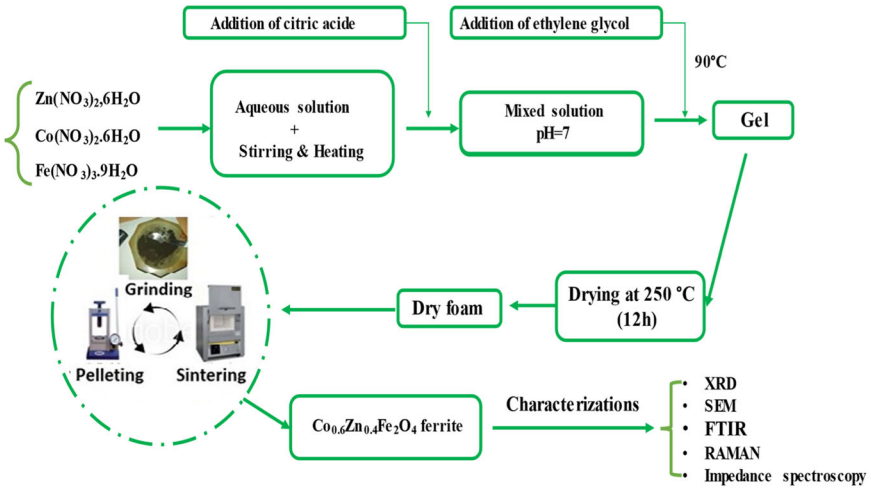

Fig. 1 Sol–gel synthesis steps for $Co_{0.6}Zn_{0.4}Fe_2O_4$ ferrite

such as lead-free composition, high Curie temperature, low dielectric loss, chemical stability, and cost-effectiveness. Unlike lead-based ceramics [27, 28], which raise environmental concerns due to lead toxicity, $Co_xZn_{1-x}Fe_2O_4$ ($x = 0.6$) is a safer and more environmentally friendly option. Additionally, its high Curie temperature makes it suitable for applications requiring temperature stability, while its low dielectric loss contributes to high energy storage efficiency and low power consumption. Furthermore, $Co_{0.6}Zn_{0.4}Fe_2O_4$ is chemically stable and resistant to degradation, making it suitable for harsh environments and long-term operation. Its cost-effectiveness compared to lead-based ceramics makes it a more economical choice for large-scale applications. $CoFe_2O_4$ is an inverse ferrimagnetic spinel with Co^{2+} ions located on octahedral sites and Fe^{3+} ions located on octahedral and tetrahedral sites. The presence of diamagnetic Zn^{2+} cations, which replace Fe^{3+} cations at tetrahedral sites, is expected to improve the saturation magnetization while having minimal impact on the electrical response [29, 30]. The objective of this study is to synthesize and analyze Zn–Co nanoferrites using the sol–gel method. This method is preferred over other synthesis techniques due to its advantages such as reduced time and power consumption, relatively lower operating temperature, better uniformity, and lower cost [29]. Despite the potential of Zn–Co nanoferrites, there has been limited investigation into their morphological and electrical properties as reported in the literature.

2 Experimental details

2.1 Preparation of $Co_{0.6}Zn_{0.4}Fe_2O_4$ ferrite

The sol–gel process was used to synthesize the $Co_{0.6}Zn_{0.4}Fe_2O_4$ spinel ferrite. Because of its potential benefits such as improved uniformity, lower treatment temperatures, shorter annealing periods, higher purity, and improved material properties, this approach has been successfully employed to produce high-quality compounds. We used metal nitrate reagent grade chemicals $Fe(NO_3)_2{\cdot}9H_2O$ (Sigma-Aldrich, 99.9%), $Zn(NO_3)_2{\cdot}6H_2O$ (Sigma-Aldrich, 98%), and $(NO_3)_2{\cdot}4H_2O$ (Sigma-Aldrich, 99.9%) and ethylene glycol ($C_2H_6O_2$, 99%), for the synthesis of our compound.

The process of synthesizing the $Co_{0.6}Zn_{0.4}Fe_2O_4$ nanoferrite is illustrated in Fig. 1. Metal nitrates were weighed and uniformly dissolved in 100 ml of distilled water using stoichiometric quantities. The solution was then placed on a stirring plate at 90 °C in a fume hood to form a sol. Citric acid was added as a fueling agent at a molar ratio of 1:3 for the metal nitrates. Ethylene glycol was added as a polymerization agent, and the mixture was stirred and heated for 2 h until a dark gel was formed. The gel was dried at 200 °C and then calcined at 400 °C for 24 h. The last powder was milled, calcined at 600 °C for 24 h, and then calcined at 700 °C for another 24 h. The finished powder was milled once again, calcined for 24 h at 600 °C, and then calcined again for 24 h at 700 °C. The granular material was then formed into pellets using a 10 tonne/cm^2 press, with a thickness and diameter of 1 and 10 mm, respectively. The pellets were sintered for 24 h at 1000 °C to obtain the desired crystalline phase of the $Co_{0.6}Zn_{0.4}Fe_2O_4$ nanoferrite. The resulting pellets were carefully ground, pelletized, ground again, and sintered for 12 h at 1000 °C.

2.2 Characterization techniques

For X-ray diffraction (XRD) analysis, a minimal amount of material, ~0.2 g, was finely powdered and uniformly dispersed on the sample holder. The XRD pattern was collected at room temperature over a 2θ range of 10°–80° employing a Bruker 8D Advance X-ray powder

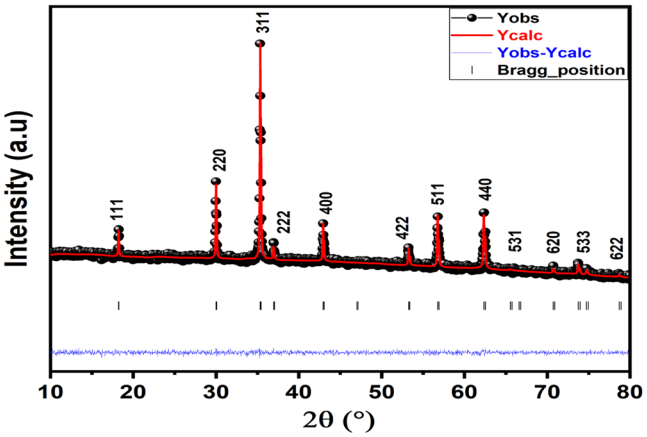

Fig. 2 XRD pattern with Rietveld refinement for $Co_{0.6}Zn_{0.4}Fe_2O_4$. The underneath line (blue) depicts the difference between the XRD data (black) and calculated fit (red), and the green lines are Bragg positions

diffractometer, equipped with monochromatized Cu-Kα radiation (wavelength $\lambda = 1.5406$ Å). Rietveld refinement was employed to optimize the XRD data, utilizing the Foolproof tool for determining cell parameters, phase purity, and homogeneity of the synthesized sample. The material's morphology was examined using a TESCAN VEGA3 SBH scanning electron microscope (SEM) with a BurkerXFlagh 410 M EDS detector. Several spectroscopic techniques were performed to investigate the properties of the product. Raman spectroscopy, using a Raman microsystem (Horiba LabRam HR Evolution) with an excitation wavelength of 532 nm, an open-space confocal microscope, a CCD detector, and a 600 gmm^{-1} grating, was utilized to determine the spinel structure and study its vibrational motions. Fourier transform infrared (FTIR) spectroscopy was conducted on the sample using a Bruker-Tensor-37 spectrometer, covering a wavenumber range of 400–4000 cm^{-1}. Absorbance (A) and reflectance (R) were calculated based on these measurements. Finally, impedance measurements were carried out in the frequency range of 100 Hz–3 MHz using an Agilent 4294 network analyzer.

3 Results and discussions

3.1 XRD pattern analysis

Figure 2 displays the Rietveld XRD pattern of the $Co_{0.6}Zn_{0.4}Fe_2O_4$ sample refined powder using Foolproof software, revealing planes (111), (220), (311), (222), (400), (422), (511), (440), (531), (620), (533), and (622). These confirm the formation of a monophasic spinel structure with the space group Fd-3m. The Bragg peak profile was described using the pseudo-Voight function. No additional reflections were observed at the Bragg peaks corresponding to any other phase than spinel ferrite, as demonstrated in the diffractogram [31]. Additionally, the standard JCPDS card number 22-1086 of the pure cobalt spinel ferrite structure $CoFe_2O_4$ events and the indexed Miller's indices for diffraction peaks are in good accord [31]. The XRD pattern's broad lines are explained by the crystallites' nanometer-scale dimensions.

Furthermore, the broadening of the XRD pattern's lines hints at the nanoscale dimensions of the crystallites within the sample. Such broadening is often indicative of small particle sizes, which lead to an increase in the line width due to the XRD size effect. The Rietveld refinement process not only confirms the phase purity and structure but also yields vital quantitative data about the sample. Parameters such as the lattice constants and the reliability factor are deduced from the refinement and encapsulated in Table 1. These parameters are crucial for understanding the crystallography of the synthesized material and for confirming its expected properties and potential applications in various fields. Crystallographic parameters are pivotal in affirming the anticipated properties and potential applications of synthesized materials, particularly in fields like magnetic storage or sensor technology. These parameters offer detailed insights into the structural characteristics of the material, significantly influencing its behavior and functionalities. For instance, unit cell dimensions and atomic positions, key crystallographic parameters, play a crucial role in confirming the structural integrity and stability of the material. This confirmation is particularly vital for applications where material stability, such as in magnetic storage or sensors, is of utmost importance.

The lattice distances between planes (*hkl*) were deduced from the XRD pattern using the formula given in Eq. (1).

$$d_{hkl} = \frac{n\lambda}{2\sin\theta} \tag{1}$$

In this equation, λ is the incident radiation ($\lambda = 1.5406$ Å), n is the order of reflection and θ is the diffraction angle,

Table 1 Structural parameters of $Co_{0.6}Zn_{0.4}Fe_2O_4$ ferrite, as extracted from the structural refinement report using the Rietveld method

Structure			$Co_{0.6}Zn_{0.4}Fe_2O_4$
Space group			Fd-3m
Cell parameters	a (Å)		8.418 (6)
	V (Å^3)		596.61 (7)
Atoms	A-Site Fe/Zn	Wyckoff positions	16d
		Atomic positions $x = y = z$	0.125
		Occupancy factors	0.6/0.4
		B_{iso} (Å^2)	1.48 (2)
	B-Site Fe/Co	Wyckoff positions	8a
		Atomic positions $x = y = z$	1/2
		Occupancy factors	1.4/0.6
		B_{iso} (Å^2)	1.17 (3)
	O	Wyckoff positions	32e
		Atomic positions $x = y = z$	0.2587 (8)
		Occupancy factors	4
		B_{iso} (Å^2)	2.02 (4)
Structural parameters	R_A (Å)		1.948 (2)
	R_B (Å)		2.035 (2)
	$\theta_{A\text{-}O\text{-}B}$ (°)		122.4 (1)
	$\theta_{B\text{-}O\text{-}B}$ (°)		94.0 (1)
Agreement factors	R_p (%)		1.58
	R_{wp} (%)		1.94
	R_F (%)		4.76
	χ^2 (%)		1.06

According to Eq. (2), a (the lattice constant) is estimated from the maximum peak (corresponding to diffraction angle ($2\theta = 35.332°$) and (311) plane direction) [32]:

$$a = \frac{\lambda}{2}\frac{\sqrt{h^2+k^2+l^2}}{\sin\theta} \tag{2}$$

The X-ray density for our compound was calculated using the next Eq. (3) [33]:

$$D_X = \frac{8M}{Na^3} \tag{3}$$

In equation 3, where 8 denotes the number of molecules in a unit cell, M is the sample's molecular weight, its lattice constant, and N is Avogadro's number.

The equation was used to get the bulk density (4) [34].

$$D_b = \frac{m}{h\pi r^2} \tag{4}$$

The pellet's mass is m, its radius is r, and its thickness is h. According to Eq. (5), the percentage porosity was calculated as follows [35]:

$$P = \left(1 - \frac{D_b}{D_X}\right) \times 100 \tag{5}$$

The calculated value lattice parameter, bulk density, X-ray density, and porosity are 8.42 Å, 5.28, 4.86 g cm^{-3}, and 7.92% respectively. Pores are formed as a result of sintering, which explains the discrepancy between X-ray density and bulk density [36]:

The mean crystallite size was initially estimated using the standard Scherer method, which entails using the Scherer formula presented in Eq. (6) [37, 38]:

$$D_{SC} = \frac{k\lambda}{\beta\cos\theta} \tag{6}$$

In equation 6, where k is a constant ($k = 0.89$), λ the wavelength of the X-ray radiation, β the full width at half maximum of the most intense peak (311) given in radians, and θ is the diffraction angle. The average crystallite size in our sample is 47.4 nm.

3.2 Elemental and morphological analysis

The fracture microstructure image of $Co_{0.6}Zn_{0.4}Fe_2O_4$ ferrite was analyzed by SEM. The SEM illustration and agglomeration of grains distribution of our sample are shown in Fig. 3a, b. The SEM image clearly illustrates the distinct chemical contrast of the ferrite phase. Additionally, it displays the non-uniform surface behavior of the regularly shaped agglomeration of grains, which exhibit large facets. The presence of black dots indicates the porosity of the sample. This porosity is likely a result of the sintering process. During sintering, the particles in the sample are heated to a high temperature, causing them to fuse together and form a solid body. However, if the sintering temperature is too low or the sintering time is too short, the particles may not fully fuse together, resulting in the formation of pores. The presence of porosity can affect the electrical and magnetic properties of the material. For example, porosity can reduce the density of the material, which can lead to a decrease in its magnetic permeability. Additionally, porosity can provide a path for the movement of ions, which can increase the conductivity of the material. To confirm the presence of porosity, we measured the density of the sample using the Archimedes method. The measured density is 5.28 g/cm^3. This value is lower than the theoretical density of $Co_{0.6}Zn_{0.4}Fe_2O_4$ ferrite (5.45 g/cm^3), which confirms the presence of porosity in the sample.

Moreover, the SEM image of the investigated compound closely resembles those of pure or doped spinel ferrite systems prepared using other methods such as solid-state, auto combustion, coprecipitation, and microwave

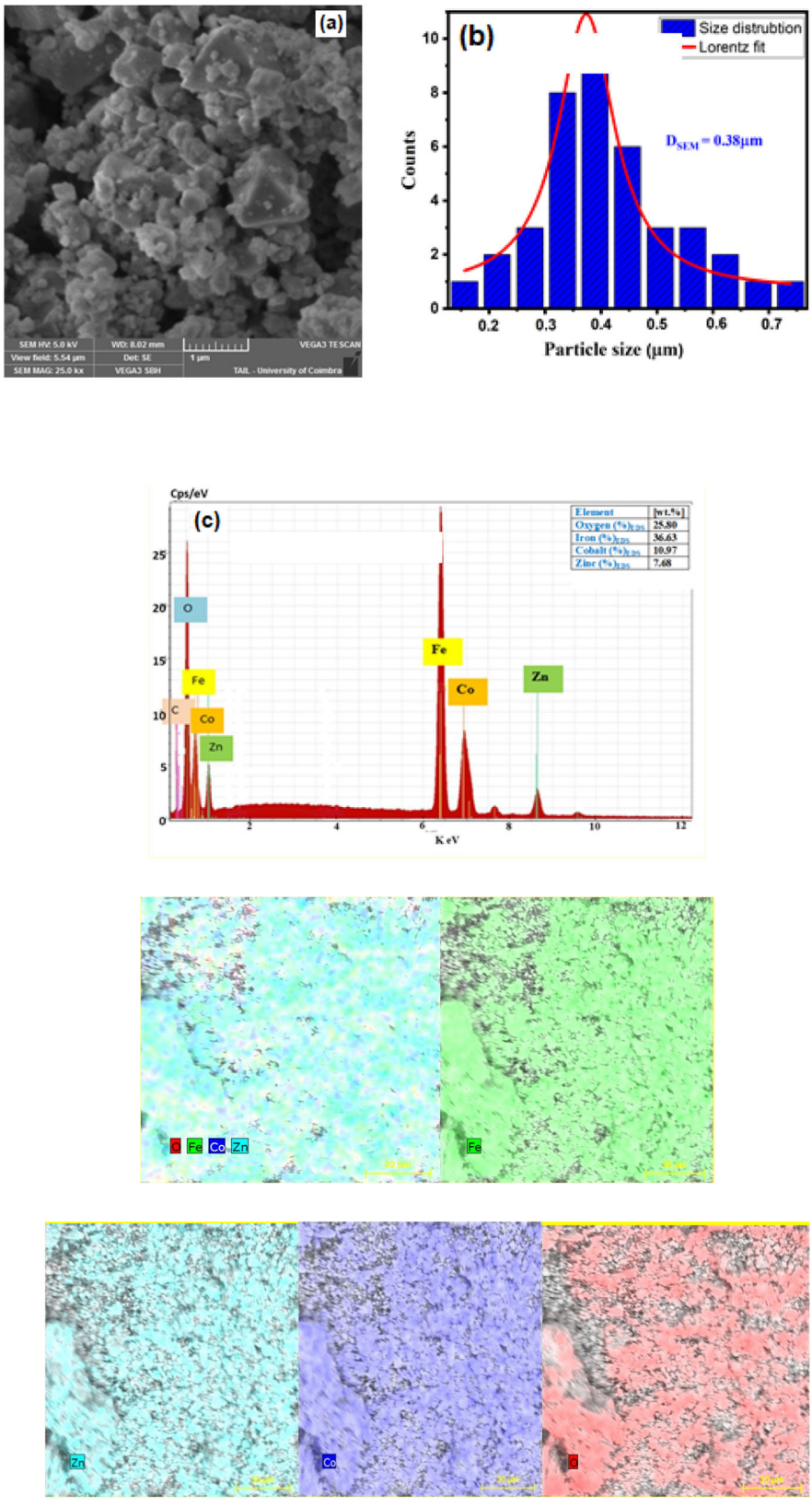

Fig. 3 SEM image (**a**), grains size distribution (**b**), and EDS spectrum (**c**) for $Co_{0.6}Zn_{0.4}Fe_2O_4$ ferrite

irradiation methods [39–42]. In previous studies, researchers have observed large agglomerates with small particles adhering to their surfaces, similar to what is observed in our SEM image. Manual statistical granularity counts were conducted using ImageJ software to analyze grain size agglomeration distribution. The distribution was effectively modeled by the Lorentz function, represented by the solid red line in the histogram. The Lorentzian fit revealed a prominent population of agglomerates centered at 0.38 µm. The disparity can be attributed to the unique characteristics of SEM analysis, which allows for the examination of agglomeration of grains containing a considerable number of much smaller crystallites. Figure 3c presents EDS spectrum and corresponding elemental mapping of $Co_{0.6}Zn_{0.4}Fe_2O_4$. These results verify the absence of any missing elements or extraneous impurities during the reaction process. Additionally, the EDS map demonstrates an even dispersion of all elements across the connection face. The EDS spectrum exhibits distinct peak intensities corresponding to Co, Zn, Fe, and O elements, providing evidence of their presence. The dominant elements identified in the sample include Oxygen (25.8%), Iron (36.6%), Cobalt (11%), and Zinc (7.7%). The percentage composition values obtained from the EDS analysis offer quantitative insights into the relative abundance of each element. Iron emerges as a significant component, constituting the highest percentage among the identified elements. Cobalt and Zinc also contribute noticeably to the overall composition, confirming their presence in the material. Oxygen, as expected, constitutes a substantial proportion, reflecting the oxides and compounds in the sample.

These results verify the absence of any missing elements or extraneous impurities during the reaction process. Additionally, the EDS map demonstrates an even dispersion of all elements across the connection face.

3.3 FTIR analysis

For wavenumbers between 100 and 1000 cm^{-1}, the infrared band of solids is typically attributed to the vibration of ions in the crystal lattice [43, 44]. All spinals, especially ferrites, exhibit two important infrared absorption bands. The highest υ_1 is generally observed in the range 550–600 cm^{-1}, corresponding to the intrinsic stretching mode of the metal at the tetrahedral position $M_{tetra} \leftrightarrow O$, and the other υ_2 is observed in the range 350–400 cm^{-1} corresponding to the stretching mode of the metal at the octahedral position $M_{octa} \leftrightarrow O$ [45]. Nanoparticles of $Co_{0.6}Zn_{0.4}Fe_2O_4$ were characterized by FTIR spectroscopy at 400–4000 cm^{-1}. In Fig. 4, two bands at 434 and 572 cm^{-1} show that cation–anion interactions (metal–oxygen) are present at octahedral and tetrahedral sites of $Co_{0.6}Zn_{0.4}Fe_2O_4$ [46, 47]. The ~760 cm^{-1} band is a typical vibrational peak for nitrate species. This confirms the presence of NO_3 during the synthesis process [48].

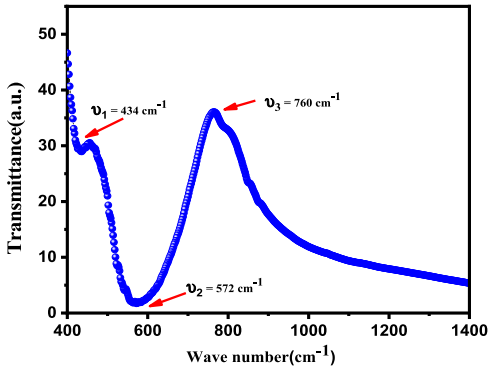

Fig. 4 Room temperature FTIR spectrum for $Co_{0.6}Zn_{0.4}Fe_2O_4$ ferrite spinel

3.4 Conductivity studies

Verwey and Boer proposed that in ferrites, electrons are exchanged between ions of the same element with multiple valence states, which are randomly distributed on equivalent sites in the lattice [49]. This exchange of electrons is also responsible for the electronic transition from Fe^{3+} to Fe^{2+} ions, which is an important factor for conduction in ferrites [50, 51]. The electrical conductivity σ of $Co_{0.6}Zn_{0.4}Fe_2O_4$ sample was calculated from the relation [52]:

$$\sigma = G\frac{t}{A} \tag{7}$$

In the given equation, G represents the electrical conductance, A denotes the cross-sectional area of the pellet, and t represents its thickness. The conductivity behavior of $Co_{0.6}Zn_{0.4}Fe_2O_4$ with respect to temperature (300–500 K) and frequency (100 Hz–3 MHz) is shown in Fig. 5a.

As the temperature increases, the conductivity (σ) also rises, indicating a thermally activated conduction process. Notably, the conductivity exhibits two distinct behaviors that are dependent on the frequency [53, 54]:

(1) At low frequencies, the conductivity remains constant up to ~1000 Hz for a given temperature, signifying a homogeneous conductance attributed to the direct current conductivity (σ_{dc}).

(2) At higher frequencies, the conductivity demonstrates an increase, suggesting an additional influx of charge carriers and enhanced carrier hopping mechanisms between consecutive sites within the material. This phenomenon is characterized by a dispersion behavior known as AC conductivity (σ_{ac}).

The underlying mechanisms responsible for the increase in conductivity with increasing temperature can be

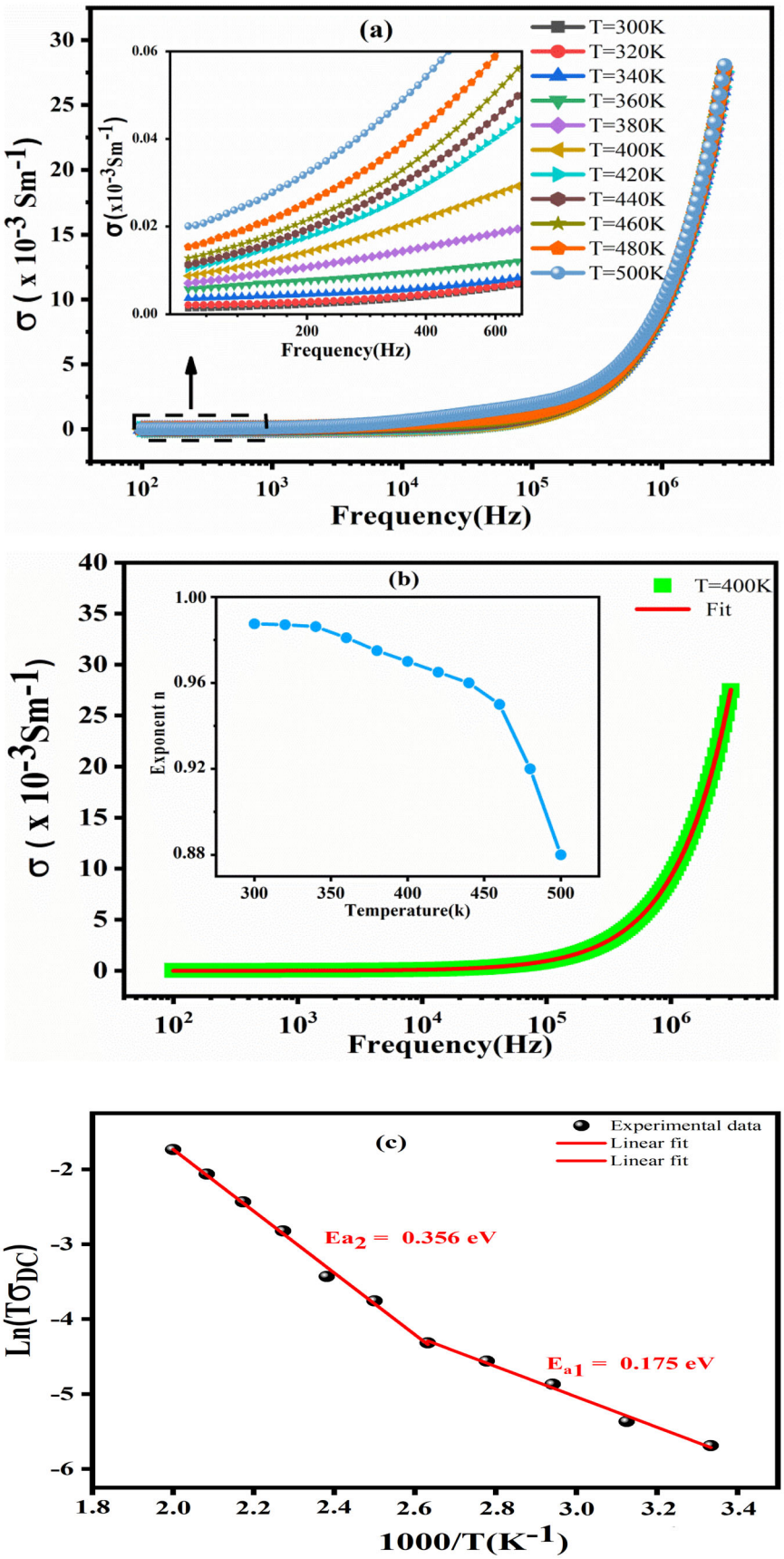

Fig. 5 Frequency dependency of the total conductivity at different temperatures for $Co_{0.6}Zn_{0.4}Fe_2O_4$ ferrite (**a**). Representative example (conductivity versus frequency at $T = 400$ K) fitted using the Jonscher law. The inset depicts the variation of the exponent s as a function of the temperature (**b**). Plot of $\mathrm{Ln}(T\sigma_{DC})$ versus $1000/T$ (**c**)

Table 2 Fitting parameters of the conductivity of $Co_{0.6}Zn_{0.4}Fe_2O_4$ ferrite

T (K)	A	B	n
300	$1.252\ 10^{-6}$	$1.090\ 10^{-9}$	0.9872
320	$1.988\ 10^{-6}$	$1.085\ 10^{-8}$	0.9875
340	$2.000\ 10^{-6}$	$1.087\ 10^{-8}$	0.9874
360	$2.033\ 10^{-6}$	$1.091\ 10^{-8}$	0.9873
380	$2.087\ 10^{-6}$	$1.099\ 10^{-8}$	0.9868
400	$2.748\ 10^{-6}$	$1.116\ 10^{-8}$	0.9861
420	$1.115\ 10^{-5}$	$1.117\ 10^{-8}$	0.9861
440	$4.408\ 10^{-5}$	$1.124\ 10^{-8}$	0.98522
460	$7.361\ 10^{-5}$	$1.142\ 10^{-8}$	0.9848
480	$1.189\ 10^{-4}$	$1.201\ 10^{-8}$	0.9815
500	$1.858\ 10^{-4}$	$1.329\ 10^{-8}$	0.9746

explained by various models, such as the hopping model, the band model, or the variable range hopping model. The specific mechanism that dominates in a particular material depends on factors such as the type of charge carriers, the density of localized states, and the temperature range.

Furthermore, the electrical conductivity adheres to Jonscher's law [55, 56]:

$$\sigma = \sigma_{dc} + \sigma_{ac} = \sigma_{dc} + A\omega^n \tag{8}$$

In this equation, A is a constant; σ_{ac} and σ_{dc} are the alternating current and direct current conductivity, respectively; $\omega = 2\pi f$; and n is a dimensionless factor that characterizes the interaction between mobile charge carriers and their environment. It is commonly used to describe the electrical conductivity of glasses, amorphous semiconductors, and ionic conductors [57].

By way of equation (9), all the curves of the variations of conductivity with frequency and temperature are fitted in order to evaluate σ_{dc}, A and the exponent n listed in Table 2 are the fitting parameters. The obtained exponent n values for the temperature range of 300–500 K fall between 0.987 and 0.883; these results indicate that the conduction mechanism aligns with the correlated barrier hopping (CBH) model, suggesting a concerted movement of charge carriers influenced by correlated interactions within the material's barriers [52]. The CBH model takes into account the cooperative movement of charge carriers and the energy barriers involved in the hopping process. In this mechanism, charge carriers hop between localized states, but their motion is influenced by the interactions with other charge carriers and the surrounding lattice. This leads to a dispersive AC conduction behavior, where the conductivity depends on the frequency of the applied electric field. The variation of the exponent n with temperature, as shown in the inset of Fig. 5b, provides further evidence for the CBH mechanism. As the temperature increases, the value of n decreases, indicating a transition from a more AC-dominated conduction mechanism at lower temperatures to a more direct current (DC)-like conduction mechanism at higher temperatures. This behavior is consistent with the thermally activated nature of the conduction process, where the increased thermal energy of the charge carriers at higher temperatures allows them to overcome the potential barriers more easily.

The exponent n according to the CBH model is given by ref. [52].

$$n = 1 - \frac{6K_BT}{W_m} \tag{9}$$

The binding energy of polaron at the site of localization of a charge carrier is defined as W_m. As a first step in understanding the relaxation process, we analyze the conductivity response at different temperatures. Figure 5c depicts $\mathrm{Ln}(T\sigma_{dc})$ versus $1000/T$ at different temperatures in the range of 300–500 K. In both regions, the curves are linear, confirming the thermal activation (T_A) of conduction.

Mott and Davis' law can be used to explain the experimental results regarding the dc conductivity:

$$\sigma_{dc}T = \sigma_0 \exp\left(-\frac{E_a}{K_BT}\right) \tag{10}$$

In this equation, σ_0 represents a pre-exponential factor, K_B represents Boltzmann's constant, E_a is a symbol for activation energy and T represents absolute temperature. The values of E_a are determined via the slope of Ln ($\sigma_{dc}.T$) versus $1000/T$ in Fig. 5c. For the temperature range between 300 to 380 K the value of $E_{a1} = 0.175$ eV and $E_{a2} = 0.356$ eV for the temperature range between 400 to 500 K; these values are similar to these of the E_a in the spinel ferrites [58]. The mechanism behind conduction in nanoferrites has been explained using Verwey and De Boer's theory [59], which proposes that electrons exchange between identical-element ions that have different valence states. This electron exchange between Fe^{2+} and Fe^{3+} can produce n-type carriers, while hole exchange between Co^{3+} and Co^{2+} as well as Zn^{2+} and Zn^{1+} can produce p-type carriers in spinel ferrites [60–63]. The composition of the nanoferrites can account for this phenomenon. Within the context of Co–Zn nanoferrites, octahedral sites predominantly host Co^{2+} ions, while tetrahedral sites are primarily occupied by Zn^{2+} ions. Additionally, both octahedral and tetrahedral sites accommodate Fe ions.

3.5 Complex impedance analysis

The dielectric material's complex impedance is shown below:

$$Z^* = Z' - jZ'' \tag{11}$$

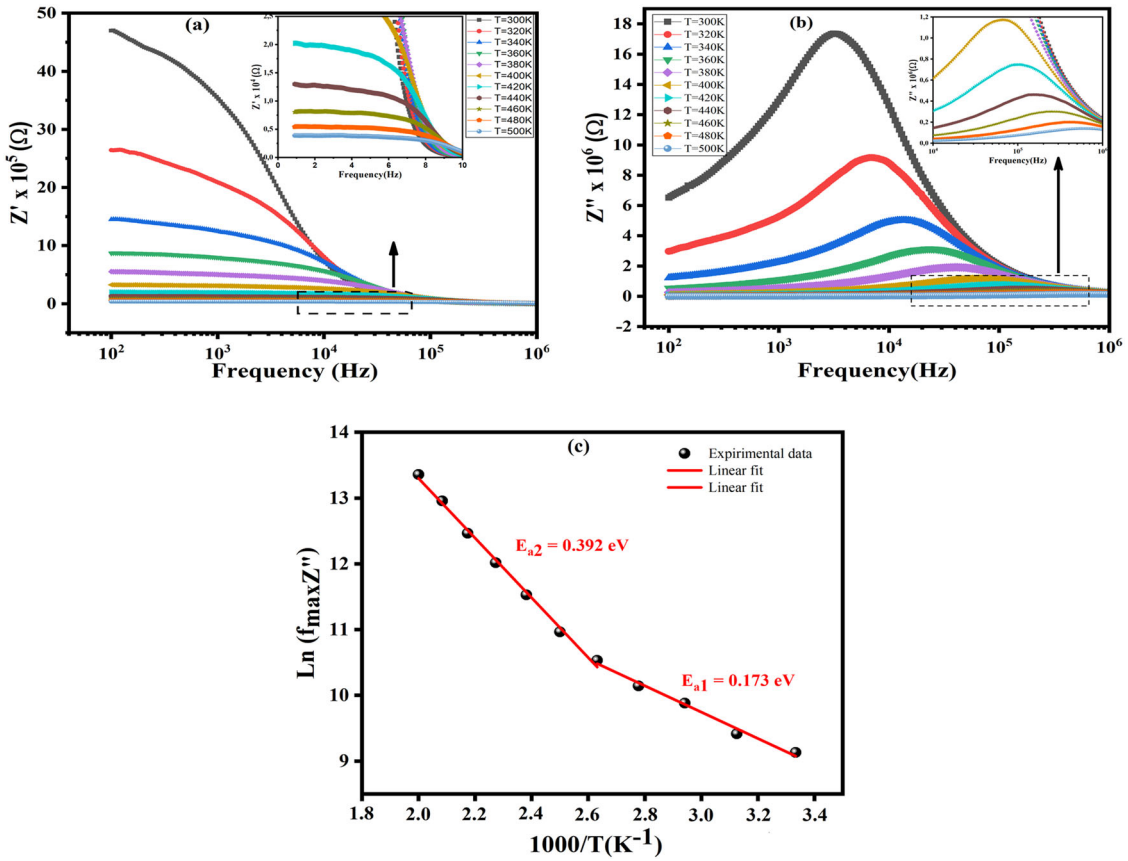

Fig. 6 Variation in the real part of the impedance Z' (**a**), imaginary part of the impedance Z'' (**b**) with the frequency at various temperatures, and variation of $\ln(f_{maxZ''})$ versus $1000/T$ (**c**) for $Co_{0.6}Zn_{0.4}Fe_2O_4$ ferrite spinel

where Z' and Z'' represent the real and imaginary parts of the complex impedance, respectively.

The variations in the real Z' and imaginary Z'' parts as a function of frequency are shown in Fig. 6a, b for temperatures ranging from 300 to 500 K. Z' appears to be practically constant in the low-frequency band, but it falls as frequency and temperature rise. This suggests that the behavior is thermally activated. The Z' increases at the lower frequency limit with decreasing temperature, which can be explained by the decrease in AC conductivity that occurs when charge transporter mobility and trapped charge density increase [64]. At higher frequencies, Z' rapidly declines and converges to a constant value. This can be attributed to the increased AC conductivity in this region due to the release of fixed charges and the decrease in the density of trapped charges [65]. Additionally, the Z'' spectrum approaches a maximum, indicating the presence of relaxation frequencies associated with grains [66], as illustrated in Fig. 6b. With increasing temperature, the peak progressively shifts to higher frequencies, suggesting the occurrence of a relaxation process driven by thermal activation. In order to determine the activation energy of the $Co_{0.6}Zn_{0.4}Fe_2O_4$ compound, we plot the fluctuation of $\ln(f_{maxZ''})$ versus $1000/T$ as shown in Fig. 6c, where $f_{maxZ''}$ is the frequency at which the Z''_{max} occurs; the resultant curve obeys the following Arrhenius law:

$$f_{max\,Z''} = f_0 \exp\left(-\frac{E_a}{K_B T}\right) \tag{12}$$

wherein E_a is the activation energy, $K_B = 8.625\ 10^{-5}$ eV K^{-1} is the Boltzmann constant, f_0 is a pre-exponential factor, and T is the temperature under consideration. The activation energy values found are $E_{a1} = 0.173$ eV and $E_{a2} = 0.392$ eV. It is worth noting that these values are very close to the results of DC conductivity studies. Accordingly, the energy barrier between conduction and relaxation must be crossed by charge carriers.

Complex Z'' versus Z' impedance curves (called Nyquist plots) of $Co_{0.6}Zn_{0.4}Fe_2O_4$ at different temperatures are shown in Fig. 7a characterizing the contributions of grains, grain boundaries, and electrodes [67]. The Nyquist plot of Z' versus Z'' in an ideal dielectric demonstrates Debye relaxation as a semicircle or series of semicircles. However, in most solids with various flaws, the relaxation mechanism is non-Debye, resulting in an asymmetrical or barely concave semicircle, indicating alternative relaxation and

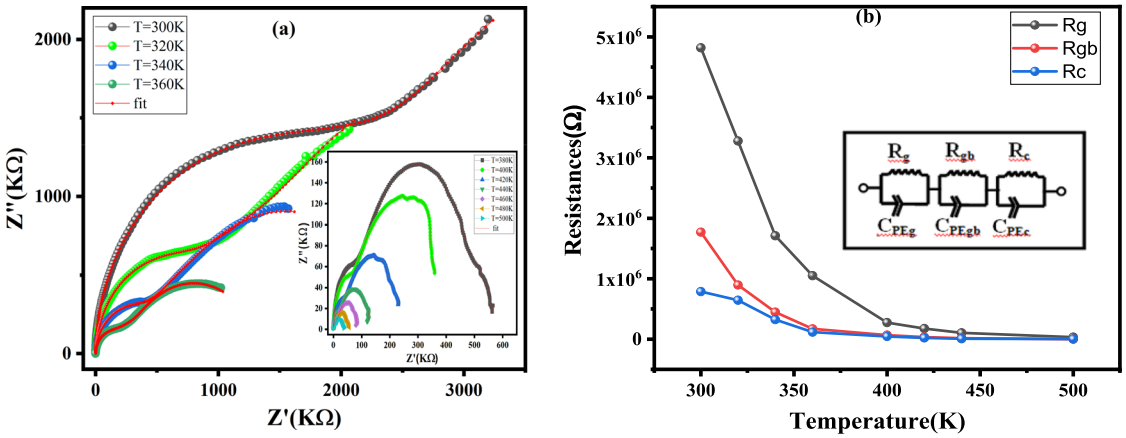

Fig. 7 Nyquist plot (**a**) and variation of resistances R_g, R_{gb}, and R_c versus temperature (inset equivalent circuit) (**b**) for $Co_{0.6}Zn_{0.4}Fe_2O_4$ ferrite

Table 3 Equivalent circuit electrical parameters obtained from complex impedance spectra of $Co_{0.6}Zn_{0.4}Fe_2O_4$ sample at different temperatures

T (K)	R_g (KΩ)	C_{PEg} (nF)	α_g	R_{gb} (KΩ)	$C_{PEgb}(10^{-2}$ nF)	α_{gb}	R_c (KΩ)	C_{PEc} (nF)	α_c
300	4820	0.711	1.010	1770	8.63	0.986	786.460	0.482	1.010
320	3277	0.998	1.001	895	8.44	0.985	645	0.672	0.999
340	1710	0.999	0.988	447.480	8.71	0.984	323.380	0.897	0.989
360	1050	1.870	0.884	170.760	7.89	1.003	116.500	0.502	1.002
380	754.345	2.106	0.865	92.427	8.59	0.991	73.384	0.836	0.968
400	274.170	1.860	0.919	67.151	9.43	0.983	45.445	1.760	0.972
420	175.730	3.200	0.853	34.710	8.21	0.998	21.795	1.610	0.951
440	103.810	4.240	0.811	16.129	6.81	1.020	7.852	0.878	0.984
460	71.126	5.160	0.802	8.812	6.71	1.025	5.084	0.753	0.971
480	52.945	8.360	0.781	3.245	4.01	1.041	3.946	0.076	1.048
500	33.119	11.900	0.732	1.147	1.06	1.184	2.877	0.031	1.122

conduction mechanisms [68]. In the temperature range of 380–500 K, the presence of three semicircular arcs is visible, and their maximum values decrease with increasing temperature. This phenomenon is attributed to the enhanced movement of charge carriers at elevated temperatures. The greater mobility of these carriers results in a higher concentration, ultimately causing the observed reduction in the semicircle's diameter.

Three semicircular arcs indicate that there have been three relaxing occurrences [69]. The dispersion conduct of Z'' at the Z' axis is explained by the Cole-Cole model, in which the complex impedance Z^* is given by the relation [70]:

$$Z*(\omega) = \frac{\mathrm{R}}{1 + (\frac{j\omega}{\omega_0})^{1-n}} \tag{13}$$

For $n = 0$, the standard Debye formalism is obtained. The dispersion in the Nyquist drawing is due to the material's heterogeneity: electrodes, grain boundaries, and grains. At temperatures below 360 K, the three different semicircles merge into two, indicating that one or both of the two effects are overlapping. Zview software [71] was used to simulate the impedance data. In the inset of Fig. 7b, the equivalent circuit diagram for $Co_{0.6}Zn_{0.4}Fe_2O_4$ is shown. The equivalent circuit is built up of three parallel circuits linked up by a resistor R and a constant-phase element CPE in each. The impedance of the CPE is given by the following relationship [72].

$$Z_{\mathrm{CPE}} = [\mathrm{A}(j\omega)^{\alpha}]^{-1} \tag{14}$$

where ω is the angular frequency, A is a scale factor, and α is an exponent ranging from 0 to 1. The CPE is considered an ideal capacitive element at $\alpha = 1$, while it corresponds to resistance at $\alpha = 0$. The parameter values obtained by fitting to different temperatures are summarized in Table 3. The resistances versus temperature curves are presented in Fig. 7b. The variation of resistance values with temperature provides insights into the conduction mechanism and charge transport in the ferrite. In general, the resistance of a material decreases with increasing temperature due to the increased thermal energy of the charge carriers. It can be observed that the resistances R_g, R_{gb}, and R_c decrease with

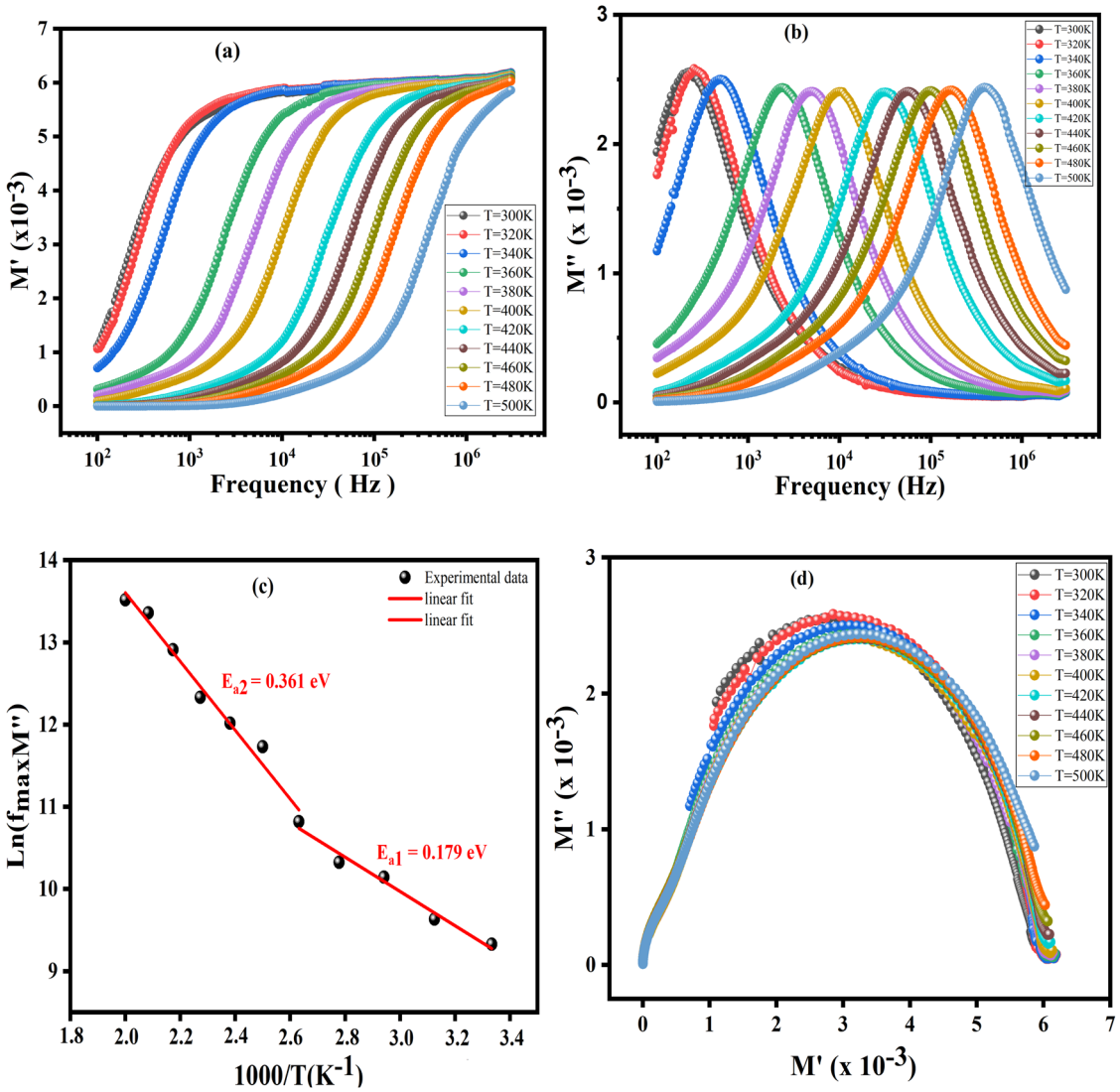

Fig. 8 Variation in the real part of the electrical modulus M' (**a**), imaginary part of the electrical modulus M'' (**b**) with the frequency at various temperatures, plot of $\ln(f_{\max M''})$ versus $1000/T$ (**c**) and Argand plot of $Co_{0.6}Zn_{0.4}Fe_2O_4$ ferrite spinel (**d**)

increasing temperature. This trend indicates that charge transport in all three domains, namely electrodes, grains, and grain boundaries, is thermally activated. The decrease in resistance suggests an increase in the mobility of charge carriers in the sample [73].

3.6 Modulus study

To understand the dielectric characteristics of the prepared sample, complex electrical modulus formalism is required. The complex electric modulus (M^*) was determined as follows:

$$M^*(\omega) = M'(\omega) + jM''(\omega) = j\omega C_0 Z^* \quad (15)$$

where $M' = \omega C_0 Z''$ and $M'' = j\omega C_0 Z'$ are the real and imaginary portions of the complex electrical modulus, respectively; $j = (-1)^{1/2}$; $\omega = 2\pi f$ is the angular frequency; and $C_0 = \varepsilon_0 A/t$ is the geometrical capacitance with $\varepsilon_0 = 8.854 \times 10^{-12}$ F/m being the permittivity of free space, A is the surface area and t is the thickness of the sample [74]. The frequency dependences of the imaginary M'' (b) and real components of the modulus M' (a) at various temperatures are presented in Fig. 8, as is the variation of ln ($f_{\max M''}$) versus $1000/T$ from modulus data (c), and the Argand plot (d) of $Co_{0.6}Zn_{0.4}Fe_2O_4$ ferrite in the temperature range 300 to 500 K. At low frequencies, the value of M' is low but not zero, as seen in Fig. 8a. This finding implies that the influence of the electrodes cannot be overlooked. The curve of M' achieves a constant value equal to $M\infty$ at high frequencies. Figure 8b is worth noting that the M'' curve peaks at a frequency known as the relaxation frequency ($f_{\max M''}$). As the temperature increases, this

maximum value shifts to the high-frequency region. This behavior implies that dielectric relaxation is thermally generated and that carrier hopping activities are inherently dominating in the grains [75].

The variation of the relaxation frequency with the inverse of temperature (Ln($f_{maxM''}$) against 1000/T) is shown in Fig. 8c. We notice that this variation presents an activated behavior according to the Arrhenius relation [76]:

$$f_{\max M''} = f_0 \exp\left(-\frac{E_a}{K_B T}\right) \quad (16)$$

The fitted curve activation energy values are 0.179 and 0.361 eV, which are in good agreement with the values determined by DC conduction. The Argand diagram of electrical modulus (M'' versus M') for the $Co_{0.6}Zn_{0.4}Fe_2O_4$ sample at diverse temperatures is displayed in Fig. 8d. We discovered a solitary semicircle related to the grain effect. The semicircle changes from a closed semicircle to an arc as the temperature rises. The existence of non-semicircles in the figure M'' against M' shows non-Debye type relaxation.

3.7 Dielectric study

Dielectric spectroscopy research can provide information about a dielectric material's compound structure, grain boundaries, grains, transport parameters, and charge storage capacities [77]. The following equation can be used to determine a material's dielectric response:

$$\varepsilon^*(\omega) = \varepsilon'(\omega) + j\varepsilon''(\omega) = \frac{1}{j\omega C_0 Z^*} \quad (17)$$

where $j = (-1)^{1/2}$; $\omega = 2\pi f$; $C_0 = \varepsilon_0 A/t$ (geometrical capacitance) with $\varepsilon_0 = 8.854 \times 10^{-12}$ F/m being the permittivity for free space; A is the surface area; t is the sample thickness; and the terms $\varepsilon'(\omega)$ and $\varepsilon''(\omega)$ are the real and imaginary parts of the dielectric permittivity, describing respectively the energy storage and loss in the material. The dielectric loss, tanδ, is correlated to the dielectric relaxation process and is given as the fraction of the imaginary part ε'' and the real part ε', i.e., $\tan\delta = \varepsilon''/\varepsilon'$. The variations of the real part (ε') of the permittivity and the imaginary part (ε'') of the relative dielectric constant (ε'') of the $Co_{0.6}Zn_{0.4}Fe_2O_4$ as a function of frequency at various temperatures are shown in Fig. 9a, b. From the inspection of these data (ε') and (ε'') decrease with increasing frequency until very low values, then they stay almost constant, but increase with temperature at a given frequency which agrees well with preceding publications [78]. The dielectric constant, on the other hand, is extremely high at low frequencies. This demonstrates that space charge polarization exists at grain boundaries, creating a potential barrier. The behavior of charge accumulation at grain boundaries is another factor that contributes to an increase in the real component of the dielectric permittivity [79]. This phenomenon can be explained by Koop's hypothesis, which is in line with the Maxwell–Wagner model [80–82]. According to this theory, ferrite materials consist of highly conductive grains separated by less conductive grain boundaries. Grain boundaries are more active in the low-frequency range than grains in terms of conduction [83]. When an electric field is applied to the ferrite, electrons (Fe^{2+}–Fe^{3+}) emerge, controlling the polarization. At low frequencies, space charge polarization occurs when electrons accumulate at poorly conductive grain boundaries, leading to high ε' values. However, as the frequency increases, electron exchange between Fe^{2+} and Fe^{3+} ions cannot keep up with the alternating field, reducing the probability of electrons reaching the grain boundaries, and thus decreasing polarization. On the other hand, the dielectric loss (tanδ) reflects energy dissipation in a dielectric system and is proportional to the imaginary component of the dielectric constant [84] Dielectric loss is the energy loss caused by grain boundaries when polarization lags behind the applied electric field. In dielectric materials, dielectric losses are induced by three independent causes: space charge transport (contribution to interface polarization), DC conduction, and molecule dipole motion (dipole losses) [85]. Figure 9c illustrates the frequency dependence of the dielectric loss tan at various temperatures. The permittivity (ε'') curves exhibit the same tendency.

The high value of tanδ at low frequencies can be attributed to the high resistivity of grain boundaries, which are more efficient than grains.

The novelty of the $Co_{0.6}Zn_{0.4}Fe_2O_4$ ferrite lies in its excellent dielectric properties, making it a promising candidate for various electronic devices. The dielectric constant of $Co_{0.6}Zn_{0.4}Fe_2O_4$ is significantly higher than that of other state-of-the-art ferrites (Table 4), and it exhibits a low dielectric loss, particularly suitable for high-frequency applications such as antennas and sensors.

A comparison table of its dielectric constant and loss with other ferrites shows that its properties are comparable to or better than those of other leading ferrites, further highlighting its potential for practical applications. This research contributes to the development of new ferrite materials with improved properties, addressing the increasing demand for high-performance electronic devices. The structural and magnetic properties of $Co_{0.6}Zn_{0.4}Fe_2O_4$ have been studied extensively, demonstrating its potential for various applications in the field of electronic materials.

We have complemented the quantitative analysis with graphical insights, tracing the curves of both dielectric constant and dielectric loss. These visual representations, showcased in Fig. 10, offer a nuanced perspective on the electrical behavior of the $Co_{0.6}Zn_{0.4}Fe_2O_4$ ferrite, enriching our understanding of its performance characteristics.

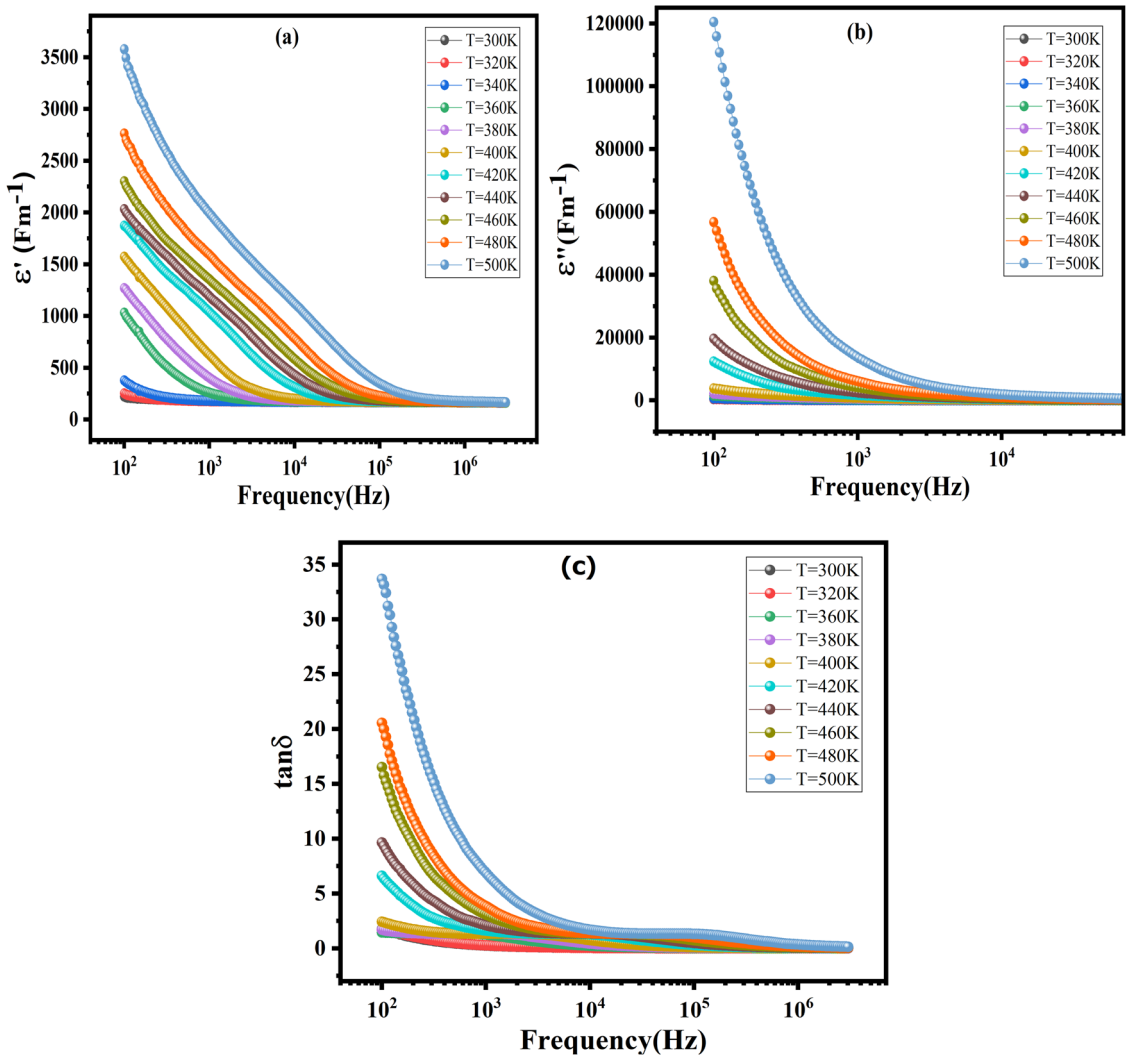

Fig. 9 Variation in the real part of the dielectric constant ε' (**a**), imaginary part of the dielectric constant ε'' (**b**), and the dielectric loss tanδ with the frequency at various temperatures for $Co_{0.6}Zn_{0.4}Fe_2O_4$ ferrite spinel (**c**)

Table 4 Comparative analysis of dielectric constant and loss for $Co_{0.6}Zn_{0.4}Fe_2O_4$ and state-of-the-art ferrites

Material	Dielectric constant	Dielectric loss	Reference
$Co_{0.6}Zn_{0.4}Fe_2O_4$	12.5	0.02	This work
$NiFe_2O_4$	14.0	0.04	[86]
$CoFe_2O_4$	10.5	0.03	[87]
$MnFe_2O_4$	11.0	0.05	[88]
$Co_{0.5}Zn_{0.5}Fe_2O_4$	13.5	0.025	[89]
$Co_{0.7}Zn_{0.3}Fe_2O_4$	14.5	0.035	[90]
$Co_{0.8}Zn_{0.2}Fe_2O_4$	15.0	0.040	[91]

The temperature dependence of the dielectric loss and constant of $Co_{0.6}Zn_{0.4}Fe_2O_4$ ferrite was investigated in the frequency range of 100 Hz–3 MHz and the temperature range of 300–500 K. The dielectric constant (ε') and dielectric loss (tanδ) of the material exhibit distinct temperature-dependent behaviors, shedding light on the intricate interplay between thermal effects and electrical properties. At lower temperatures, ε' is notably high, facilitated by the ease of dipole alignment in response to the electric field, owing to reduced thermal agitation. As temperature rises, however, the increasing thermal agitation disrupts dipole alignment, leading to a decrease in ε'.

Concomitantly, the dielectric loss (tanδ) follows a similar temperature-dependent trend. At lower temperatures, tanδ remains low, as thermal agitation is insufficient to activate loss mechanisms. With increasing temperature, heightened thermal agitation activates more loss mechanisms, such as polarization and conduction, resulting in an elevation of tanδ. In essence, both ε' and tanδ exhibit analogous variations, reaching their respective maxima around T_c, underscoring the profound

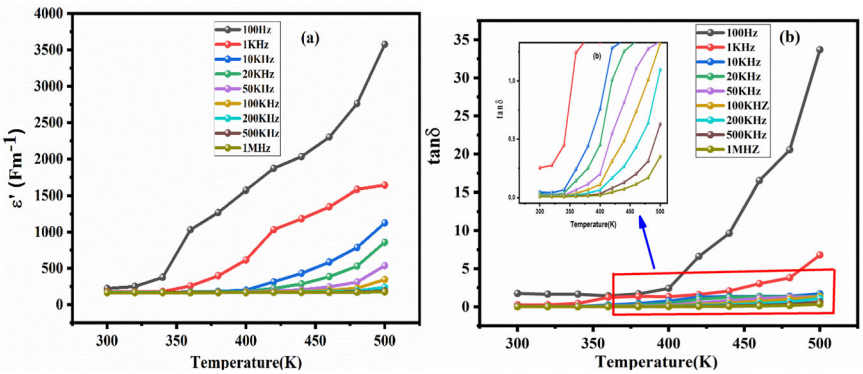

Fig. 10 Temperature dependence of dielectric constant (**a**) and loss (**b**) in $Co_{0.6}Zn_{0.4}Fe_2O_4$ ferrite

influence of thermal agitation on these crucial electrical properties. These observations highlight the direct dependence of ε' and tanδ on temperature, emphasizing its impact on dipole and charge carrier mobility within the material.

4 Conclusion

This study provides a thorough understanding of the structural, morphological, and electrical features of $Co_{0.6}Zn_{0.4}Fe_2O_4$ spinel ferrite, which was effectively synthesized utilizing the sol–gel method. The XRD analysis confirmed the formation of a monophasic spinel structure, indicating the high purity and crystallinity of the synthesized ferrites. The SEM analysis revealed a distinctive microstructure with significant grain agglomeration and porosity, characteristic of the spinel ferrite system. The FTIR spectroscopy reveals characteristic absorption bands indicating interactions between cations and anions at both tetrahedral and octahedral sites. Electrical studies revealed that the $Co_{0.6}Zn_{0.4}Fe_2O_4$ ferrite exhibits a thermally activated conduction process, in line with Jonscher's universal power law. The impedance analysis pointed to a complex interaction between grains and grain boundaries, influenced by temperature. The Nyquist plots underscored the significant contribution of these components to the overall electrical behavior of the ferrites. The modulus and dielectric studies highlighted the ferrites' efficient charge storage capabilities and low energy dissipation, making them suitable for various high-frequency applications. The low dielectric loss, in particular, positions these materials as promising candidates for applications in fields like energy storage, electronics, and telecommunications. Overall, the $Co_{0.6}Zn_{0.4}Fe_2O_4$ nanoferrites synthesized in this study exhibit a range of desirable electrical and structural properties, affirming their potential for technological advancements in various applications. The synthesis method proved to be efficient, offering a pathway for producing high-quality nanoferrites with controlled properties.

Data availability

No datasets were generated or analyzed during the current study.

Acknowledgements This work was supported by the Tunisian Ministry of Higher Education and Scientific Research with the collaboration of national funds from FCT – Fundação para a Ciência e a Tecnologia, I.P., within the project UID/04564/2020. Access to TAIL-UC facility funded under QREN-Mais Centro Project No. ICT_2009_02_012_1890 is gratefully acknowledged. This work was funded by the Researchers Supporting Project No. RSP2024R243 at King Saud University, Riyadh, Saudi Arabia.

Author contributions Authors statement conceptualization: Messaoudi. Data curation: Omri, Benali. Formal analysis: M.A. Ghebouli, M. Fatmi. Methodology: Hamdaoui, Ajjel, M. Habila. Software: Djemli, Alothman, Mohammad. Validation: Costa, Graca. Visualization: Khirouni. Roles/writing – original draft: M. Fatmi. Writing – review editing: A. Djemli.

Compliance with ethical standards

Conflict of interest The authors declare no competing interests.

References

1. Omri A, Dhahri E, Costa BFO, Valente MA (2020) Structural, electric and dielectric properties of $Ni_{0.5}Zn_{0.5}FeCoO_4$ ferrite prepared by sol-gel. J Magn Magn Mater 499:166243
2. Omri A, Dhahri E, Costa BFO, Valente MA (2021) Study of structural, morphological, Mössbauer and dielectric properties of $NiFeCoO_4$ prepared by a sol gel method. J Sol Gel Sci Technol 98:364–375
3. Kanwal M, Ahmad I, Meydan T, Cuenca J, Williams P, Farid M, Murtaza G (2018) Structural, magnetic and microwave properties of gadolinium-substituted Ca-Ba M-type hexagonal ferrites. J Electron Mater 47:5370–5377
4. Farid HMT, Ahmad I, Ali I, Ramay SM, Mahmood A (2019) Study of spinel ferrites with addition of small amount of metallic elements. J Electroceram 42:57–66

5. Hathout AS, Aljawish A, Sabry BA, El-Nekeety AA, Roby MH, Deraz NM, Aly SE, Abdel-Wahhab MA (2017) Synthesis and characterization of cobalt ferrites nanoparticles with cytotoxic and antimicrobial properties. J Appl Pharm Sci 7:086–092
6. Oumezzine E, Hcini S, Baazaoui M, Hlil E-K, Oumezzine M (2015) Structural, magnetic and magnetocaloric properties of $Zn_{0.6-x}Ni_xCu_{0.4}Fe_2O_4$ ferrite nanoparticles prepared by Pechini sol-gel method. Powder Technol 278:189–195
7. Hcini S, Selmi A, Rahmouni H, Omri A, Bouazizi ML (2017) Structural, dielectric and complex impedance properties of $T_{0.6}Co_{0.4}Fe_2O_4$ (T = Ni, Mg) ferrite nanoparticles prepared by sol gel method. Ceram Int 43:2529–2536
8. Saini A, Kumar P, Ravelo B, Lallechere S, Thakur A, Thakur P (2016) Magneto-dielectric properties of doped ferrite based nanosized ceramics over very high frequency range. Eng Sci Technol Int J 19:911–916
9. Horchani M, Omri A, Benali A, Eddine MS, Tozri A, Dhahri E, Graca M, Valente M, Jakka S, Costa B (2022) Synthesis and investigation on the microstructural and electrical proprieties of $Ni_{0.1}Co_{0.5}Cu_{0.4}Fe_2O_4$ ferrite prepared using sol-gel route. J Solid State Chem 308:122898
10. Fang M, Ström V, Olsson RT, Belova L, Rao KV (2011) Rapid mixing: a route to synthesize magnetite nanoparticles with high moment. Appl Phys Lett 99:222501.
11. Sickafus KE, Wills JM, Grimes NW (1999) Structure of spinel. J Am Ceram Soc 82:3279–3292
12. Aneeta Manjari P, Mary PR, Sanjib N, Sugato H, Manisha S, Zvonko J, Hoe Joon K (2023) Synthesis and application of mixed-spinel magnesioferrite: structural, vibrational, magnetic, and electrochemical sensing properties. Mater Chem Front 7:72–84
13. Nayak S, Ghorai S, Padhan AM, Hajra S, Svedlindh P, Murugavel P (2022) Cationic redistribution induced spin-glass and cluster-glass states in spinel ferrite. Phys Rev B 106(17):174402
14. Oh W, Hajra S, Divya S, Panda S, Oh Y, Jaglic Z, Phakkhananan P, Oh TH, Hoe Joon K (2023) Contact electrification of porous PDMS-nickel ferrite composites for effective energy harvesting. Mater Sci Eng B 292:116397
15. Bhargava H, Lakshmi N, Sebastian V, Reddy V, Venugopalan K, Gupta A (2009) Investigation of the large magnetic moment in nano-sized $Cu_{0.25}Co_{0.25}Zn_{0.5}Fe_2O_4$. J Phys D Appl Phys 42:245003
16. Chiu W, Radiman S, Abd-Shukor R, Abdullah M, Khiew P (2008) Tunable coercivity of $CoFe_2O_4$ nanoparticles via thermal annealing treatment. J Alloys Compd 459:291–297
17. Meaz T, Attia S, El Ata AA (2003) Effect of tetravalent titanium ions substitution on the dielectric properties of Co–Zn ferrites. J Magn Magn Mater 257:296–305
18. Köseoğlu Y, Baykal A, Gözüak F, Kavas H (2009) Structural and magnetic properties of $Co_xZn_{1-x}Fe_2O_4$ nanocrystals synthesized by microwave method. Polyhedron 28:2887–2892
19. Duong GV, Turtelli RS, Hanh N, Linh D, Reissner M, Michor H, Fidler J, Wiesinger G, Grössinger R (2006) Magnetic properties of nanocrystalline $Co_{1-x}Zn_xFe_2O_4$ prepared by forced hydrolysis method. J Magn Magn Mater 307:313–317
20. Arulmurugan R, Vaidyanathan G, Sendhilnathan S, Jeyadevan B (2005) Preparation and properties of temperature-sensitive magnetic fluid having $Co_{0.5}Zn_{0.5}Fe_2O_4$ and $Mn_{0.5}Zn_{0.5}Fe_2O_4$ nanoparticles. Phys B Condens Matter 368:223–230
21. Hcini S, Omri A, Boudard M, Bouazizi ML, Dhahri A, Touileb K (2018) Microstructural, magnetic and electrical properties of $Zn_{0.4}M_{0.3}Co_{0.3}Fe_2O_4$ (M = Ni and Cu) ferrites synthesized by sol–gel method. J Mater Sci Mater Electron 29:6879–6891
22. Sutka A, Gross K, Mezinskis G, Bebris G, Knite M (2011) The effect of heating conditions on the properties of nano-and microstructured Ni–Zn ferrite. Phys Scr 83:025601
23. Nayak P (2008) Synthesis and characterization of cadmium ferrite. Mater Chem Phys 112:24–26
24. Shobana M, Rajendran V, Jeyasubramanian K, Kumar NS (2007) Preparation and characterisation of NiCo ferrite nanoparticles. Mater Lett 61:2616–2619
25. Mallapur M, Shaikh P, Kambale R, Jamadar H, Mahamuni P, Chougule B (2009) Structural and electrical properties of nanocrystalline cobalt substituted nickel zinc ferrite. J Alloys Compd 479:797–802
26. Azadmanjiri J, Salehani H, Barati M, Farzan F (2007) Preparation and electromagnetic properties of $Ni_{1-x}Cu_xFe_2O_4$ nanoparticle ferrites by sol–gel auto-combustion method. Mater Lett 61:84–87
27. Sujoy S, Ram Prakash S, Ashish R, Aditya M, Amanat A, Himalay B, Rajeev R (2023) Inducing ferromagnetism and magnetoelectric coupling in the ferroelectric alloy system $BiFeO_3$–$PbTiO_3$ via additives. J Appl Phys 133:064101
28. Sahu M, Pradhan SK, Hajra S, Panigrahi BK, Choudhary RNP (2019) Studies of structural, electrical, and excitation performance of electronic material: europium substituted $0.9(Bi_{0.5}Na_{0.5}TiO_3)$–$0.1(PbZr_{0.48}Ti_{0.52}O_3)$. J Appl Phys 125:183
29. Duong GV, Turtelli RS, Nunes W, Schafler E, Hanh N, Grössinger R, Knobel M (2007) Ultrafine $Co_{1-x}Zn_xFe_2O_4$ particles synthesized by hydrolysis: effect of thermal treatment and its relationship with magnetic properties. J Non Cryst Solids 353:805–807
30. Arulmurugan R, Jeyadevan B, Vaidyanathan G, Sendhilnathan S (2005) Effect of zinc substitution on Co–Zn and Mn–Zn ferrite nanoparticles prepared by co-precipitation. J Magn Magn Mater 288:470–477
31. Tahar LB, Basti H, Herbst F, Smiri L, Quisefit J, Yaacoub N, Grenèche J, Ammar S (2012) $Co_{1-x}Zn_xFe_2O_4$ ($0 \le x \le 1$) nanocrystalline solid solution prepared by the polyol method: characterization and magnetic properties. Mater Res Bull 47:2590–2598
32. Köseoğlu Y, Alan F, Tan M, Yilgin R, Öztürk M (2012) Low temperature hydrothermal synthesis and characterization of Mn doped cobalt ferrite nanoparticles. Ceram Int 38:3625–3634
33. Anwar M, Ahmed F, Koo BH (2014) Enhanced relative cooling power of $Ni_{1-x}Zn_xFe_2O_4$ ($0.0 \leqslant x \leqslant 0.7$) ferrites. Acta Mater 71:100–107
34. Mahmood A, Warsi MF, Ashiq MN, Ishaq M (2013) Substitution of La and Fe with Dy and Mn in multiferroic $La_{1-x}Dy$-$Fe_{1-y}Mn_yO_3$ nanocrystallites. J Magn Magn Mater 327:64–70
35. Abdeen A, Hemeda O, Assem E, El-Sehly M (2002) Structural, electrical and transport phenomena of Co ferrite substituted by Cd. J Magn Magn Mater 238:75–83
36. Ahmed M, Afify H, El Zawawia I, Azab A (2012) Novel structural and magnetic properties of Mg doped copper nanoferrites prepared by conventional and wet methods. J Magn Magn Mater 324:2199–2204
37. Hcini S, Zemni S, Triki A, Rahmouni H, Boudard M (2011) Size mismatch, grain boundary and bandwidth effects on structural, magnetic and electrical properties of $Pr_{0.67}Ba_{0.33}MnO_3$ and $Pr_{0.67}Sr_{0.33}MnO_3$ perovskites. J Alloys Compd 509:1394–1400
38. Kaur N, Kaur M (2014) Processing and application of ceramics. Proc Appl Ceram 8(3):137–143
39. Sozeri H, Durmus Z, Baykal A (2012) Structural and magnetic properties of triethylene glycol stabilized $Zn_xCo_{1-x}Fe_2O_4$ nanoparticles. Mater Res Bull 47:2442–2448
40. López-Ortega A, Lottini E, Fernandez CdeJ, Sangregorio C (2015) Exploring the magnetic properties of cobalt-ferrite nanoparticles for the development of a rare-earth-free permanent magnet. Chem Mater 27:4048–4056
41. Singh A, Gangwar H, Dehiya B (2017) Synthesis and microstructural characterization of pure cobalt ferrite for DC electrical study. J Mater Sci Mech Eng 4:136–141
42. Zalite I, Heidemane G, Krūmiņa A, Rašmane D, Maiorov M (2017) $ZnFe_2O_4$ containing nanoparticles: synthesis and magnetic properties. Mater Sci Appl Chem 34:38–44

43. Silambarasu A, Manikandan A, Balakrishnan K (2017) Room-temperature superparamagnetism and enhanced photocatalytic activity of magnetically reusable spinel $ZnFe_2O_4$ nanocatalysts. J Supercond Nov Magn 30:2631–2640
44. Zhang Y, Chen Y, Kou Q, Wang Z, Han D, Sun Y, Yang J, Liu Y, Yang L (2018) Effects of Nd concentration on structural and magnetic properties of $ZnFe_2O_4$ nanoparticles. J Mater Sci Mater Electron 29:3665–3671
45. Manikandan A, Kennedy LJ, Bououdina M, Vijaya JJ (2014) Synthesis, optical and magnetic properties of pure and Co-doped $ZnFe_2O_4$ nanoparticles by microwave combustion method. J Magn Magn Mater 349:249–258
46. Rouessac F, Rouessac A, Cruché D, Duverger-Arfuso C, Martel A (2019) Analyse chimique-9e éd.: *Méthodes et techniques instrumentales* (Dunod)
47. Brabers V (1969) Infrared spectra of cubic and tetragonal manganese ferrites. Phys Status Solidi B 33:563–572
48. Waldron R (1955) Infrared spectra of ferrites. Phys Rev 99:1727
49. Sharifi I, Shokrollahi H (2012) Nanostructural, magnetic and Mössbauer studies of nanosized $Co_{1-x}Zn_xFe_2O_4$ synthesized by co-precipitation. J Magn Magn Mater 324:2397–2403
50. Nouri A, Zamanian A, Kazemzadeh A, Bahrevar M, Ali-Ramaji S (2014) Synthesis and characterization of cobalt zinc ferrite-chitosan core-shell nanoparticles. Int Mater Phys J 2:16–20
51. Li J, Pan Y, Qiu F, Wu Y, Guo J (2008) Nanostructured Nd: YAG powders via gel combustion: the influence of citrate-to-nitrate ratio. Ceram Int 34:141–149
52. James A, Prakash C, Prasad G (2006) Structural properties and impedance spectroscopy of excimer laser ablated Zr substituted $BaTiO_3$ thin films. J Phys D Appl Phys 39:1635
53. Hcini F, Hcini S, Wederni MA, Alzahrani B, Al Robei H, Khirouni K, Zemni S, Bouazizi ML (2022) Structural, optical, and dielectric properties for $Mg_{0.6}Cu_{0.2}Ni_{0.2}Cr_2O_4$ chromite spinel. Phys B Condens Matter 624:413439
54. Verwey E, de Boer JH (1936) Cation arrangement in a few oxides with crystal structures of the spinel type. Recl Trav Chim Pays Bas 55:531–540
55. Devan R, Kolekar Y, Chougule B (2006) Effect of cobalt substitution on the properties of nickel–copper ferrite. J Phys Condens Matter 18:9809
56. Hajlaoui ME, Dhahri R, Hnainia N, Benchaabane A, Dhahri E, Khirouni K (2019) Conductivity and giant permittivity study of $Zn_{0.5}Ni_{0.5}Fe_2O_4$ spinel ferrite as a function of frequency and temperature. RSC Adv 9:32395–32402
57. Messaoudi A, Omri A, Benali A, Ghebouli MA, Hamdaoui N, Ajjel R, Ghebouli B, Costa BFO, Graca MFP, Khirouni K (2023) Multifaceted analysis of $Co_{0.6}Zn_{0.4}Fe_2O_4$ spinel ferrite: a comprehensive investigation into optics, dielectrics. SSRN Elsevier. Preprint at https://doi.org/10.2139/ssrn.4539237
58. Chihaoui N, Dhahri R, Bejar M, Dharhi E, Costa L, Graça M (2011) Electrical and dielectric properties of the $Ca_2MnO_{4-\delta}$ system. Solid State Commun 151:1331–1335
59. Jonscher AK (1977) The 'universal' dielectric response. Nature 267:673–679
60. Harimochi H, Kitagawa J, Ishizaka M, Kadoya Y, Yamanishi M, Matsuishi S, Hosono H (2004) Observation of Jonscher law in ac hopping conduction of the electron-doped nanoporous crystal $12CaO{\cdot}7Al_2O_3$ in a THz frequency range. Phys Rev B 70:193104
61. Abdel-Wahab F, Maksoud H, Kotkata M (2005) Electrical conduction and dielectric relaxation in semiconductor $SeSm_{0.005}$. J Phys D Appl Phys 39:190
62. Hadded A, Massoudi J, Dhahri E, Khirouni K, Costa B (2020) Structural, optical and dielectric properties of $Cu_{1.5}Mn_{1.5}O_4$ spinel nanoparticles. RSC Adv 10:42542–42556
63. Verwey E, De Boer F, Van Santen J (1948) Cation arrangement in spinels. J Chem Phys 16:1091–1092
64. Chandra Babu Naidu K, Narasimha Reddy V, Sofi Sarmash T, Kothandan D, Subbarao T, Suresh Kumar N (2019) Structural, morphological, electrical, impedance and ferroelectric properties of BaO-ZnO-TiO_2 ternary system. J Aust Ceram Soc 55:201–218
65. Raghuram N, Rao TS, Naidu KCB (2019) Investigations on functional properties of hydrothermally synthesized $Ba_{1-x}Sr_xFe_{12}O_{19}$ (x= 0.0−0.8) nanoparticles. Mater Sci Semicond Process 94:136–150
66. Naidu KCB, Wuppulluri M (2018) Ceramic nanoparticle synthesis at lower temperatures for LTCC and MMIC technologies. IEEE Trans Magn 54:1–8
67. Chavan P, Naik L, Belavi P, Chavan G, Ramesha C, Kotnala R (2017) Studies on electrical and magnetic properties of Mg-substituted nickel ferrites. J Electron Mater 46:188–198
68. Khadhraoui S, Triki A, Hcini S, Zemni S, Oumezzine M (2014) Variable-range-hopping conduction and dielectric relaxation in $Pr_{0.6}Sr_{0.4}Mn_{0.6}Ti_{0.4}O_{3\pm\delta}$ perovskite. J Magn Magn Mater 371:69–76
69. Barsoukov E, Macdonald JR (2018) Impedance spectroscopy: theory, experiment, and applications. John Wiley & Sons
70. Baaziz H, Maaloul N, Tozri A, Rahmouni H, Mizouri S, Khirouni K, Dhahri E (2015) Effect of sintering temperature and grain size on the electrical transport properties of $La_{0.67}Sr_{0.33}MnO_3$ manganite. Chem Phys Lett 640:77–81
71. Nyquist H (1932) Regeneration theory. Bell Syst Tech J 11:126–147
72. Panda R, Behera D (2014) Investigation of electric transport behavior of bulk $CoFe_2O_4$ by complex impedance spectroscopy. J Alloys Compd 587:481–486
73. Amor S, Benali A, Bejar M, Dhahri E, Khirouni K, Valente M, Graça M, Al-Turjman F, Rodriguez J, Radwan A (2019) Modulation of magnetism and study of impedance and alternating current conductivity of $Zn_{0.4}Ni_{0.6}Fe_2O_4$ spinel ferrite. J Mol Struct 1184:298–304
74. Cole KS, Cole RH (1941) Dispersion and absorption in dielectrics I. Alternating current characteristics. J Chem Phys 9:341–351
75. Johnson D (2008) ZView: a software program for IES analysis. Version 2.8. Scribner Associates, Southern Pines, NC
76. Hirschorn B, Orazem ME, Tribollet B, Vivier V, Frateur I, Musiani M (2010) Determination of effective capacitance and film thickness from constant-phase-element parameters. Electrochim Acta 55:6218–6227
77. Hajlaoui ME, Dhahri R, Hnainia N, Benchaabane A, Dhahri E, Khirouni K (2020) Dielectric spectroscopy study of the $Ni_{0.2}Zn_{0.8}Fe_2O_4$ spinel ferrite as a function of frequency and temperature. Mater Sci Eng B 262:114683
78. Omri A, Bejar M, Dhahri E, Es-Souni M, Valente M, Graça M, Costa L (2012) Electrical conductivity and dielectric analysis of $La_{0.75}$ (Ca, Sr)$_{0.25}Mn_{0.85}Ga_{0.15}O_3$ perovskite compound. J Alloys Compd 536:173–178
79. Prabakar K, Narayandass SK, Mangalaraj D (2002) Impedance and electric modulus analysis of $Cd_{0.6}Zn_{0.4}Te$ thin films. Cryst Res Technol J Exp Ind Crystallogr 37:1094–1103
80. Muralidharan P, Venkateswarlu M, Satyanarayana N (2005) Acid catalyst concentration effect on structure and ion relaxation studies of Li_2O–P_2O_5–B_2O_3–SiO_2 glasses synthesized by sol–gel process. J Non Cryst Solids 351:583–594
81. Chandran A, George K (2014) Defect induced modifications in the optical, dielectric, and transport properties of hydrothermally prepared ZnS nanoparticles and nanorods. J Nanoparticle Res 16:2238
82. Arais A, Rady K, Shams M (2018) AC conductivity and dielectric properties of Mn-Zn ferrites. Bulg J Phys 45:44–53
83. Dar MA, Majid K, Batoo KM, Kotnala R (2015) Dielectric and impedance study of polycrystalline $Li_{0.35-0.5}XCd_{0.3}NiXFe_{2.35-0.5}XO_4$ ferrites synthesized via a citrate-gel auto combustion method. J Alloys Compd 632:307–320

84. Koops C (1951) On the dispersion of resistivity and dielectric constant of some semiconductors at audiofrequencies. Phys Rev 83:121
85. Wagner KW (1913) Zur theorie der unvollkommenen dielektrika. Ann Phys 345:817–855
86. Ahmed MA, El-Dek SI, Rashad MM (2011) Structural, magnetic and electrical properties of $CoFe_2O_4$ nanoparticles prepared by sol-gel auto-combustion method. J Alloys Compd 509:6171–6178
87. Mazen SA, Rashad MM, Yahia IS (2010) Structural, magnetic and electrical properties of $NiFe_2O_4$ nanoparticles prepared by sol-gel auto-combustion method. J Magn Magn Mater 324:2026–2032
88. Ahmed MA, El-Dek SI, Rashad MM (2012) Structural, magnetic and electrical properties of $MnFe_2O_4$ nanoparticles prepared by sol-gel auto-combustion method. J Alloys Compd 512:181–187
89. Mazen SA, Rashad MM, Yahia IS (2009) Structural, magnetic and electrical properties of $ZnFe_2O_4$ nanoparticles prepared by sol-gel auto-combustion method. J Magn Magn Mater 323:1598–1604
90. Mazen SA, Rashad MM, Yahia IS (2009) Structural, magnetic and electrical properties of $Co_{0.5}Zn_{0.5}Fe_2O_4$ nanoparticles prepared by sol-gel auto-combustion method. J Magn Magn Mater 323:2850–2856
91. Ahmed MA, El-Dek SI, Rashad MM (2009) Structural, magnetic and electrical properties of $Co_{0.7}Zn_{0.3}Fe_2O_4$ nanoparticles prepared by sol-gel auto-combustion method 2011. J Alloys Compd 509:4884–4890